Opto-Electronic
Advances

CN 51–1781/TN ISSN 2096–4579 (Print) ISSN 2097–3993 (Online)

Harmonic heterostructured pure Ti fabricated by laser powder bed fusion for excellent wear resistance via strength-plasticity synergy

Desheng Li, Huanrong Xie, Chengde Gao, Huan Jiang, Liyuan Wang and Cijun Shuai

Citation: Li DS, Xie HR, Gao CD, et al. Harmonic heterostructured pure Ti fabricated by laser powder bed fusion for excellent wear resistance via strength-plasticity synergy. *Opto-Electron Adv* **8**, 250043(2025).

https://doi.org/10.29026/oea.2025.250043

Received: 10 March 2025; Accepted: 16 July 2025; Published online: 16 September 2025

Opto-Electronic Advances

Article
September 2025, Vol. 8, No. 9

DOI: 10.29026/oea.2025.250043 CSTR: 32247.14.oea.2025.250043

Harmonic heterostructured pure Ti fabricated by laser powder bed fusion for excellent wear resistance via strength-plasticity synergy

Desheng Li[1], Huanrong Xie[2], Chengde Gao[1]*, Huan Jiang[1], Liyuan Wang[1] and Cijun Shuai[1,3]*

Titanium (Ti) is a promising candidate for biomedical implants due to lightweight, superior corrosion resistance and biocompatibility. Nevertheless, pure Ti is confronted with poor wear resistance which poses a profound bottleneck for orthopedic implant applications. In this work, a novel and feasible route of mechanical milling (MM) and laser powder bed fusion (LPBF) was first developed for architecting highly tunable heterostructure in pure Ti, aiming to overcome wear resistance dilemma. During MM process, a spatial core-shell heterostructure within Ti particle was triggered by manipulating gradient and intense plastic deformation, accompanied with pre-existing dislocations. In subsequent LPBF process, the highly transient-melting kinetics and localized nature effectively perpetuated grain heterogeneity, hence creating a harmonic heterostructure within consolidated pure Ti. Consequently, the heterostructured Ti exhibited an excellent enhanced wear resistance (33.7%) compared to the homogeneous counterpart, which was attributed to a marvelous strength-plasticity synergy motivated by the hetero-deformation induced strengthening and strain-hardening. Furthermore, back-stress caused by geometrical necessary dislocation pile-ups offset partial wear shear-stress, also contributing to wear resistance enhancement. This study not only provides a manoeuvrable and paradigm route to fabricate Ti with conspicuous strength-plasticity synergy and wear resistance, but also sheds light on developing and extending cutting-edge biomedical implant applications.

Keywords: laser powder bed fusion; mechanical milling; heterostructured Ti; pre-existing dislocations; wear resistance; synergistic strength-plasticity

Li DS, Xie HR, Gao CD et al. Harmonic heterostructured pure Ti fabricated by laser powder bed fusion for excellent wear resistance via strength-plasticity synergy. *Opto-Electron Adv* **8**, 250043 (2025).

Introduction

Ti is a promising metal for biomedical implant applications owing to lightweight, superior corrosion resistance and biocompatibility[1,2]. However, Ti is besieged by poor wear resistance owing to inferior plastic shear-resistance and strain-hardening capacity, thus causing premature failure upon joint friction, which poses a sizable challenge in manufacturing of wear resistant Ti orthopedic implants[3,4]. For these reasons, many strategies, including surface treatment and element doping, have been

---

[1]State Key Laboratory of Precision Manufacturing for Extreme Service Performance, College of Mechanical and Electrical Engineering, Central South University, Changsha 410083, China; [2]Dundee International Institute, Central South University, Changsha 410083, China; [3]Jiangxi Province Key Laboratory of Additive Manufacturing of Implantable Medical Device, Jiangxi University of Science and Technology, Nanchang 330013, China.

*Correspondence: CD Gao, E-mail: gaochengde@csu.edu.cn; CJ Shuai, E-mail: shuai@csu.edu.cn

Received: 10 March 2025; Accepted: 16 July 2025; Published online: 16 September 2025

proposed to improve wear resistance and long been the primary strategies for Ti implants. Inevitably, premature failure of surface modification and release of toxic ions often carry safety shortcomings, such as mechanical deterioration, osteolysis or neural disorders, during long-term service of implants. Therefore, developing an effective strategy is put forward for enhancing the wear resistance and bio-friendly form of pure Ti implants[5]. As described by the empirical Archard law, wear resistance is closely related to both strength and plasticity[6]. Generally, a high strength together with considerable plasticity can mitigate brittle destruction or premature failure by retarding the exfoliation of material and the generation of cracks, thereby contributing to high wear resistance. Nonetheless, conventional strengthening methods (such as grain refinement, second phases, etc.) are inevitably accompanied with reduced plasticity. It is known that reduced plasticity would deprive the ability to absorb energy during friction and debilitate the capacity to repeat deformations, which is detrimental to wear resistance. Therefore, it is challenging to break through the dilemma of strength-plasticity trade-off, thereby achieving outstanding wear resistance in pure Ti implants.

In this scenario, heterostructure inspired by natural materials arises at an opportune time and is characterized by heterogeneous zones (including heterogeneity of grains, phases, or compositions, etc.) with dramatically different mechanical, physical or chemical properties. This endows heterostructure with a synergistic effect in which the integrated property exceeds the prediction by the rule-of-mixtures, providing a feasible philosophy to break down conflicting performances[7–8]. For instance, the antagonism between strength and corrosion resistance in Al-based materials is an inherent challenge to design reliable structural components. Xie et al.[9] achieved a heterostructured nano-reinforced Al-based composites with heterogeneous phase interfaces between nanoplatelets and Al-matrix. This heterostructure promoted the load transfer effect of nanoplatelets and the formation of dense protective layer, which conquered the trade-off between strength and corrosion resistance for Al-based composites. Besides, Wu et al.[10] fabricated a heterostructured AlCoCrFeNi high-entropy alloy (HEA) with fine and coarse grains via a step-by-step process route of arc-melting, cold-rolling and annealing. Consequently, the HEA achieved a strength-plasticity synergy attributed to the coupling in heterogeneous regions. These seminal studies motivated an exploration to overcome the strength-plasticity trade-off and thereby enhance the wear resistance via constructing heterostructure in pure Ti implants. To date, the developed preparation processes for heterostructures, such as surface laser treatments, electrodeposition, and arc-melting and cold-rolling followed by annealing, are complicated and circumscribed for pure Ti, leading to detrimental phase transitions and microstructures[11–12]. Therefore, it is imperative to seek out effective and adaptable strategies for developing heterostructured pure Ti implants, which can precisely control the evolution and distribution of heterogeneous regions.

Mechanical milling (MM) is a severe and repeated deformation process under highly controllable energy input, and has shown potential advantages in modulating the microstructure evolution, including grain sizes[13] solid-state phase transitions[14], and elemental diffusion[15]. For instance, Parsons et al.[16] prepared highly-reinforced Al-based composite powders with tailored morphology and composition using MM. Furthermore, Li et al.[17] constructed gradient nano-grain structure within pure Cu powders by introducing severe deformation via MM. The above studies indicated that the unique nature of MM easily endows materials with particular microstructures composed of nano, refined, and gradient grains[18,19]. This provides a promising strategy for constructing and regulating heterogeneous grains in pure Ti by various energy inputs during MM, thereby overcoming the strength-plasticity trade-off. However, MM technique is geared towards powder materials which necessitates subsequent consolidation to obtain three-dimensional parts. The heterostructures in powders originating from MM process are generally in metastable states, which easily undergo phase transformation and/or grain regrowth during the subsequent consolidating process. This poses attendant complications such as the weakening or even loss of original heterogeneous features. As reported by Yao et al.[20], Mo powders treated by MM showed ultra-fine-grained (UFGed) (~100 nm) structure. Nevertheless, the constant high temperature and pressure of subsequent sintering process induced partial grain regrowth to ~11.6 μm, resulting in the noteworthy weakening of UFGed features within final sintered Mo alloys. Therefore, an appropriate consolidation avenue is essential to perpetuate the heterostructure prepared by MM into consolidated pure Ti implants for achieving synergistic performances.

As a revolutionary technique, laser powder bed fusion

(LPBF) has obtained widespread attention owing to digital, flexible, and controllable consolidation process, which opens new possibilities for the direct and fast production of metallic parts with extremely complex geometries and specific microstructure[21–22]. Moreover, the highly transient-melting kinetics and localized nature are well qualified for suppressing undesired microstructure transformations, which provides a connatural superiority for perpetuating the metastable microstructure features of powders into consolidated parts[23–24]. For instance, Jung et al.[25] fabricated amorphous Zr-based alloys via LPBF process, and found that the transformations of metastable amorphous phase within initial powders were restrained during solidification, due to the extremely rapid cooling. As studied by Li et al.[26], a hierarchical CoCrFeMnNi HEA was fabricated via LPBF by using a mixture of coarse-grained (CGed) powders and UFGed powders. They found that the large super-heating and undercooling induced by LPBF tended to suppress the regrowth of UFGs and thereby perpetuate the initial UFGed structure into HEA alloys. In summary, LPBF is extraordinarily promising to perpetuate the heterogeneous features formed in MM and thus endow a configurable heterostructure in pure Ti implants.

In this work, a novel and manoeuvrable route of MM and LPBF was proposed for architecting spatial heterostructured pure Ti implants, intending to break the strength-plasticity trade-off dilemma for achieving enhanced wear resistance. Emphases were put on the effects of MM process on the grain size, dislocations, and morphology evolutions within MMed pure Ti powders. Then, the MMed powders were consolidated by LPBF and a systematic study was conducted on the heterostructure features in the resulting pure Ti. Moreover, the wear resistance of heterostructured pure Ti was investigated in elaboration via tribological behaviour, microhardness, and strength-plasticity. The relevant reinforcement mechanisms were discussed and revealed through an in-depth analysis associated with microscopic characterizations of grain heterogeneity and dislocation distribution.

Experiments

MM and LPBF strategy

As shown in Fig. 1, a manufacturing route was used to construct heterostructured pure Ti implants. Ti powders (Grade 1) with a purity of 99.99% from Beijing Shape Memory Additive Technology Co., Ltd., China were used as initial powders in the present study. The initial powders exhibited a spherical morphology, with a particle size distribution (PSD) of 15–53 μm. The MM process (Step Ⅰ) was carried out in a high-energy planetary ball mill apparatus (Pulverisette 6, Fritsch, Germany) using tungsten carbide jar, and 304 L stainless-steel balls with Φ=6 mm in an Ar atmosphere. The ball-to-powder ratio, milling speed and time of MM process mainly determined morphology and microstructure features of MMed pure Ti powders. The impact energy transferred to powders by MM process can be calculated from[27]:

$$E_k=0.5m_b\cdot V_b^2\ , \tag{1}$$

where E_k is the kinetic energy transferred to the powders, m_b and V_b are the mass and speed of milling balls, respectively. Specially, V_b is determined using the following formula[27]:

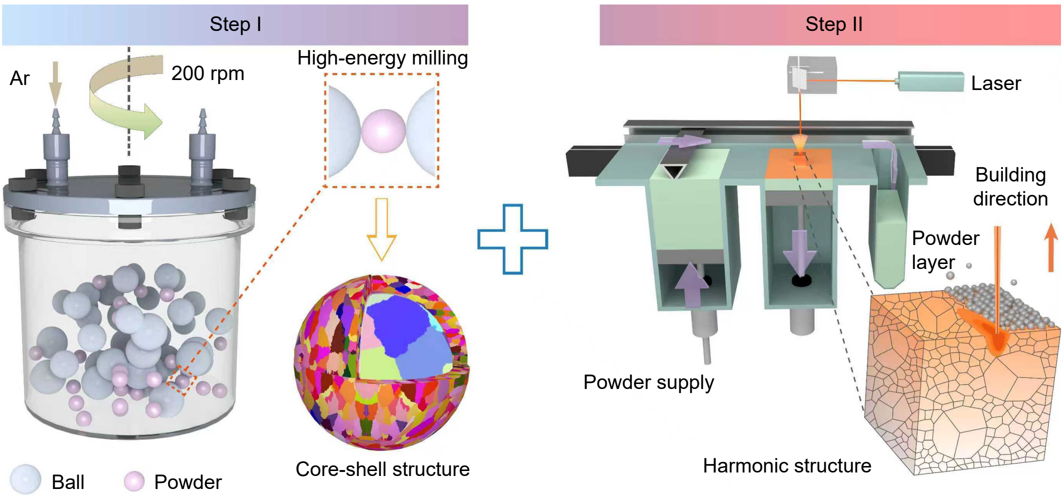

Fig. 1 | A manufacturing route of MM and LPBF for developing heterostructured pure Ti implants.

$$V_b^2 = (R\cdot\Omega)^2 + (r - r_b)\cdot\omega^2\cdot(1 + 2\omega/\Omega)\,, \qquad (2)$$

where R and Ω are the radius and angular speed of a sun wheel disk of a planetary ball mill, respectively; r and r_b are the radiuses of milling jar and ball, respectively, and ω is the angular speed of milling jar. For the MM of metal powders, such as pure Ti, Ti_6Al_4V, and Al powders, the energy approximately ranged from 30–60 W for achieving controllable microstructures[27–29]. In this work, according to the relevant studies, the ball-to-powder ratio, milling speed and time were 1:1–5:1, 120–300 rpm and 0–50 hours, respectively, for manipulating the milling energy. A series of pre-experiments indicated that ball-to-powder ratio and milling speed mainly affected the free space and instantaneous temperature during collision, and fracture and welding. Concretely, the ball-to-powder ratio influenced the collision between balls and Ti powders, and the excessively low value (1:1) significantly reduced collision effect, while the excessively high value (3:1) caused uneven collision due to the insufficient free space. Furthermore, a moderate milling speed was a key factor in obtaining a satisfying morphology of Ti powders. When the milling speed was too low (150 rpm), the balls and powders could not adequately collide with each other, thus failing to refine the grains of Ti powders. When the milling speed was too high (250 rpm), the flake shape of Ti powders became more pronounced, and powders were prone to fracture, thus forming abundant fragments. Hence, the ball-to-powder ratio and milling speed were optimized as 2:1 and 200 rpm, respectively, for achieving the satisfying morphology and particle sizes. More importantly, the milling time crucially determined the phases and grain sizes[17,29–30], and was manipulated for a desired microstructure in this work. The MM process was performed in discontinuous mode consisting of 30 min milling followed by 5 min intervals, and Ti powders milled for 0, 10, 20, and 30 hours were referred to as MM-0, MM-10, MM-20, and MM-30, respectively. As shown in Supplementary information of Fig. S1, no impurity elements were introduced into the pure Ti powder during MM by element analysis.

In subsequent process (Step Ⅱ), a series of MMed pure Ti powders were layer-by-layer consolidated into the corresponding samples via a self-developed LPBF system, named as HS-0, HS-10, HS-20, and HS-30, respectively. To obviate oxidation reaction during consolidation, the LPBF process was executed in a protective Ar atmosphere. The LPBF manufacturing system was mainly equipped with a powder spreading platform, a 500 W fiber laser, and a scanning mirror. It was emphasized that a series of LPBF pre-experiments were carried out for optimizing parameters. A moderate laser energy density (E) by manipulating laser power (P), scanning speed (V), hatch distance (H), and layer thickness (T) was conducive to satisfying consolidated quality, and E was calculated from ref.[31,32]:

$$E = P/(V\times H\times T)\,. \qquad (3)$$

Based on the self-developed LPBF system in the present work, it was found that when E was too low (approximately <105 J/mm³), Ti powders were difficult to melt completely, which led to a loose structure with edge peeling in implants. When E was too high (approximately >310 J/mm³), the excessive heat accumulation induced the generation and expansion of cracks, while leading to grain coarsening in Ti implants. Finally, the optimized parameters in the present work were determined as laser power of 190 W, scanning speed of 90 mm/s, hatch distance of 0.08 mm, and layer thickness of 0.1 mm, with laser spot size of 50 μm. The desired Ti samples were fabricated with a size of 10 mm × 10 mm × 10 mm (Supplementary information of Fig. S2).

Microstructure characterizations

To reveal the grain structure evolution, the microstructure of MMed powders and LPBFed implants was characterized through electron backscattering diffraction (EBSD, symmetry, Oxford, UK) operated at 15 kV and a scan step size of 0.3 μm. Subsequent detailed analysis of heterostructure features, including grain sizes, kernel average misorientation (KAM), and dislocation density, was performed utilizing orientation analyzing AZtecCrystal software. The prior-β grains with body-centered cubic structure were reconstructed by AZtecCrystal software based on the obtained EBSD data. Furthermore, the microstructure within MMed powders and the transverse section of LPBFed samples were observed by transmission electron microscopy (TEM, JEM-2100plus, JEOL, Japan) operated at 200 kV with energy-dispersive X-ray spectroscopy (EDS). Especially, TEM samples of the wear-scar section were prepared via a focused ion beam (FIB) system, combined with a high-angle annular dark-field (HAADF) scanning TEM (STEM) to further analyze. Subsequently, the analysis of high-resolution TEM (HRTEM) and selected area electron diffraction (SAED) patterns was carried out. A geometric phase analysis

(GPA) method was utilized to visualize atomic-level strains, thereby obtaining reliable strain distribution data. Fast Fourier Transform (FFT) and inverse FFT (IFFT) were performed using Digital Micrograph software.

Besides, PSD analysis of MMed powders was conducted using a laser particle size analyzer (Mastersizer 3000, Malvern, Netherlands) with purified water as the dispersant. Scanning electron microscopy (SEM, Phenom ProX, Phenom, Netherlands) equipped with EDS was employed to scrutinize the morphology of MMed powders. To evaluate the adaptation for subsequent LPBF process, the flowability of all MMed powders was measured at least three times using a Hall Flowmeter according to ASTM B855-17. The phase identification of all samples was undertaken utilizing X-ray diffraction (XRD, PANalytical Empyrean, Malvern, Netherlands) with a 2θ range spanning from 25° to 90° and a scan rate of 5°/min. Subsequently, the phase structure analysis of samples was carried out using HighScore Plus software.

Mechanical tests

For tensile tests, Ti samples were fabricated to dog-bone-shaped (overall length of 30 mm) via LPBF with a gage section of 15 mm × 3 mm × 1.8 mm (Supplementary information of Fig. S2). The tensile performances were assessed through tensile tests conducted using a mechanical testing apparatus (CMT5105, Sasck, China) operating at a loading speed of 0.5 mm/min. And stress-strain curves were recorded along with the exploration of fracture morphologies via SEM. For wear resistance tests, Ti samples were fabricated to 10 mm × 10 mm × 10 mm by LPBF, and then polished to attain a mirror-like surface finish. The frictional behaviour of LPBFed Ti samples was evaluated using a ball-on-sample experimental model through a friction testing machine (UMT-3, Bruker CETR, USA), with constant sliding track of 4 mm, reciprocating frequency of 2 Hz, and duration of 1800 s. The common friction pair consisting of a Si_3N_4 ball (Φ=6 mm) was adopted for the friction tests of Ti samples under varying loads of 2.5, 5, 7.5 and 10 N, respectively. Besides, ultrahigh molecular weight polyethylene (UHMW-PE) balls (Φ=6 mm) as friction pairs were also employed to explore the frictional behaviour under different working conditions. During the tests, the friction coefficients (COFs) of all samples were continuously recorded. Following the friction tests, the analysis of frictional behaviour, wear volume and surface roughness was conducted using a 3D laser scanning microscope (VHX-50000, Keyence, Japan). The microhardness tests were conducted utilizing a Vickers hardness tester (HXD-1000TM/LCD, Taiming, China) with an applied load of 2.94 N for a holding time of 15 s. To ensure reproducibility, all the mechanical tests were repeated at least 3 times at each site to ensure the accuracy of the results.

Statistical analysis

The obtained data were represented as the means ± standard deviations and analysed via the single-factor analysis of variance employing the statistical analysis GraphPad Prism software. Data were recognized as statistically significant while $p < 0.05$ (*, **, ***, and **** represented $p < 0.05$, $p < 0.01$, $p < 0.001$, and $p < 0.0001$, respectively).

Results and discussion

Powder microstructure

It was noted that among MM parameters, MM-time crucially determined grain structure, and particle sizes and morphology of powders. Therefore, this work explored the effects of MM process on the evolution of grain structure by manipulating MM-time, and microstructure characterization of pure Ti powders was presented in EBSD maps of Fig. 2. As shown in the inverse pole figure (IPF) map (Fig. 2(a)), the initial powders possessed a CGed (~6.5 μm) microstructure and spherical morphology. Upon MM treatments, grain refinement within the surface layer of particles induced by high-energy input contributed to creating shell regions composed of UFGs (~0.8 μm), as clearly observed in Fig. 2(b–d). Comparatively, the interior of MMed Ti particles still exhibited CGed structures encapsulated by the outer UFGs. As a result, a peculiar microstructure consisting of UFGed shell and CGed core regions was architected in MMed pure Ti powders and thereafter defined as core-shell heterostructure. Furthermore, as shown in the higher magnification observations (Fig. 2(e–h)), UFGed shell regions gradually thickened (marked by dotted line) with increasing MM-time from 10 h to 30 h, which suggested the tunable spatial volume of core-shell regions.

The spatial heterostructure could be attributed to the dislocation introduction on the surface layer of Ti particles via plastic deformation during MM process. Concretely, at the early stages of MM process, atomic strains were induced into the surface layer of Ti particles due to the collisions among powders, balls, and jars[33]. Severe plastic deformations occurred under the accumulated

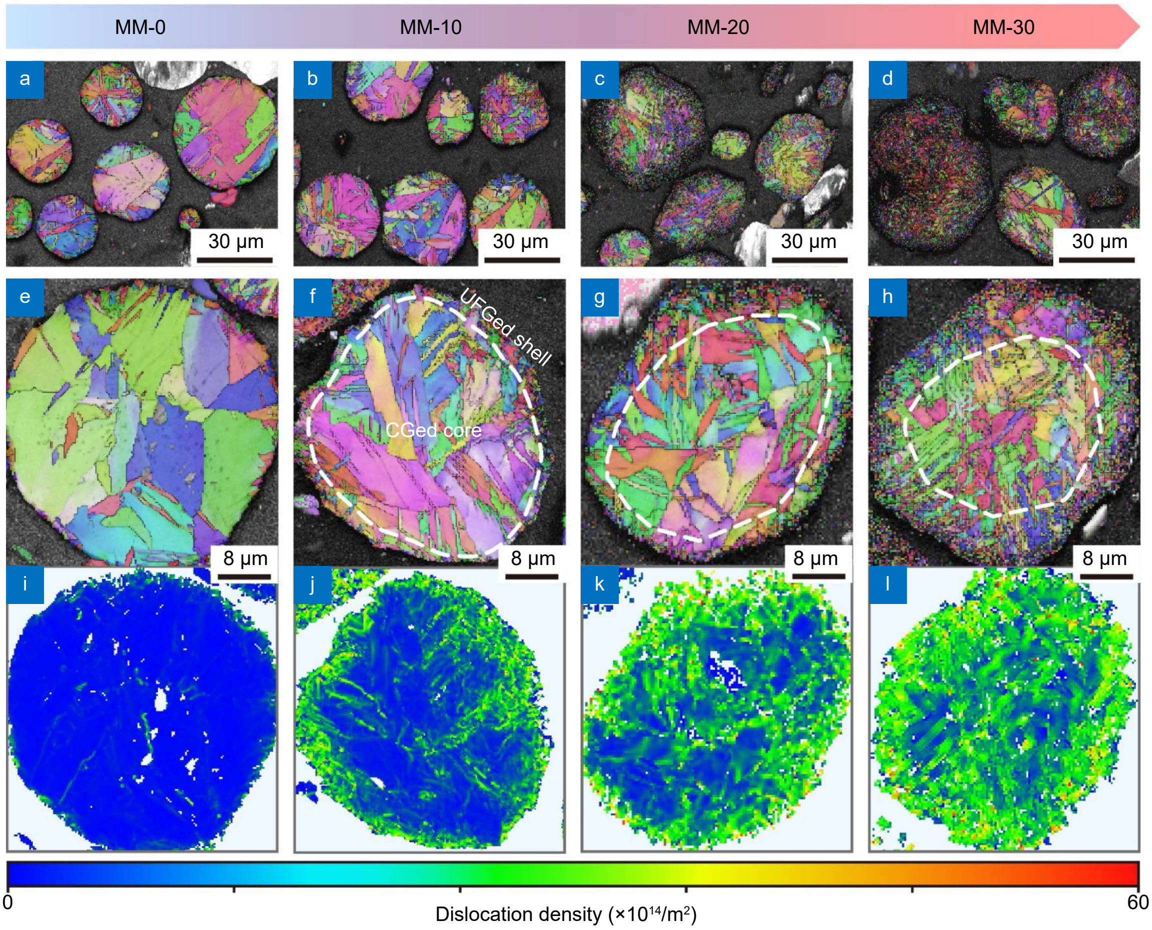

Fig. 2 | The cross-section microstructure evolution of pure Ti powders with increasing MM-time (0, 10, 20, and 30 h): (**a**–**d**) EBSD orientation maps, (**e**–**h**) magnified EBSD orientation maps, and (**i**–**l**) KAM maps.

atomic strains, which promoted the generation of abundant pre-existing dislocations. With continuous milling, the dislocation density reached a critical value and triggered dislocation walls which disintegrated the CGs into finer grains separated by grain boundaries (GBs). Consequently, the repeated and intense collisions during MM process led to the continuous grain refinement and eventual formation of UFGed shell regions on the surface of Ti particles.

In addition, KAM, defined as average misorientation between a kernel point and the neighbouring points inside individual grains, has been widely applied in dislocation density characterisations. Intuitively, dislocation density evolution within Ti powders upon different MM-time was further evaluated by KAM maps from EBSD orientation data. In Fig. 2(i), a KAM map of powders without MM process showed a thoroughly low dislocation density with entire blue regions. Divisionally, MM-10 powders were dominated by high dislocation density discriminated by green regions (Fig. 2(j)). Interestingly, the high dislocation density regions and low dislocation density regions essentially overlapped with the UFGed shell regions and CGed core regions, respectively, suggesting that the core-shell regions of heterostructure could be estimated by the dislocation density distributions. Obviously, as MM-time prolonged from 10 h to 30 h (Fig. 2(j–l)), the volumes of high dislocation density regions increased, which further confirmed the increasing thickness of UFGed shell regions. These findings demonstrated that the controllable energy input in MM process could manipulate the extent of plastic deformation and gradient distribution of grain sizes, thereby enabling development of heterostructured pure Ti powders with highly tunable volumes of core-shell regions.

To gain insights towards core-shell heterostructure, TEM characterization (Fig. 3) was further conducted on MM-20 powders as a supplement to EBSD analysis. As shown in Fig. 3(a), the obvious GBs (blue arrows) within the border layer of Ti particles further demonstrated the UFGs as outer shell regions. A HRTEM pattern of region

A suggested a heterogeneous interface (dotted line) between the core and shell regions (Fig. 3(b)). The FFT pattern (inset in Fig. 3(b)) presented a hexagonal close-packed (HCP) structure of MMed powders. Further, the SAED pattern (Fig. 3(c)) further displayed that MMed pure Ti powders were composed of a single HCP structure with representative (100), (102) and (002) lattice planes, indicating no *α*→*β* phase transformation in final pure Ti powders after MM process. As known, the *α*→*β* phase transformation requires the following conditions[34]: (I) the temperature exceeds the threshold of phase transformation (~883 °C); (II) doping abundant *β*-stabilizer to enable *β*-phase stabilization in final consolidated parts. In this work, for pure Ti powders without alloying element, MM process provided a physical driving force at low temperatures for grain refinement, which failed to meet above conditions for the *α*→*β* phase transformation. For a closer view, specific lattice fringes for core-shell regions (Fig. 3(d)) were detected in IFFT patterns of region A, demonstrating a more distinct heterogeneous interface determined by the discrepancies in the orientation of lattice fringes between core and shell regions. Furthermore, a GPA method was utilized to comprehensively probe into the nature of atomic strains, as shown in Fig. 3(e). The atomic strain along [001] reflection within MMed powders was observed to be heterogeneously distributed across the heterogeneous regions, with UFGed shell regions exhibiting an enhanced level of strain compared with the CGed core regions. This further confirmed that the collisions among powders, balls, and jars during MM process induced copious strains, which multiplied severe plastic deformation within the Ti powders. Besides, an enlarged IFFT pattern (Fig. 3(f)) at region B showed that the interplanar spacing within core and shell regions were $d_{(002)}$ = 0.234 nm and $d_{(102)}$ = 0.172 nm, respectively, which was congruent with the TEM patterns of pure Ti studied by Tao et al.[35] and further verified the SAED result of Fig. 3(c). In brief, these results demonstrated intuitively the grain heterogeneity and atomic strains triggered by MM process within the pure Ti powders.

To predict the adaptability of MMed powders for subsequent LPBF technique, the morphology evolutions of pure Ti powders for various MM-time were characterized by SEM. As shown in Fig. 4(a), the initial Ti powder particles presented a spherical morphology, with the

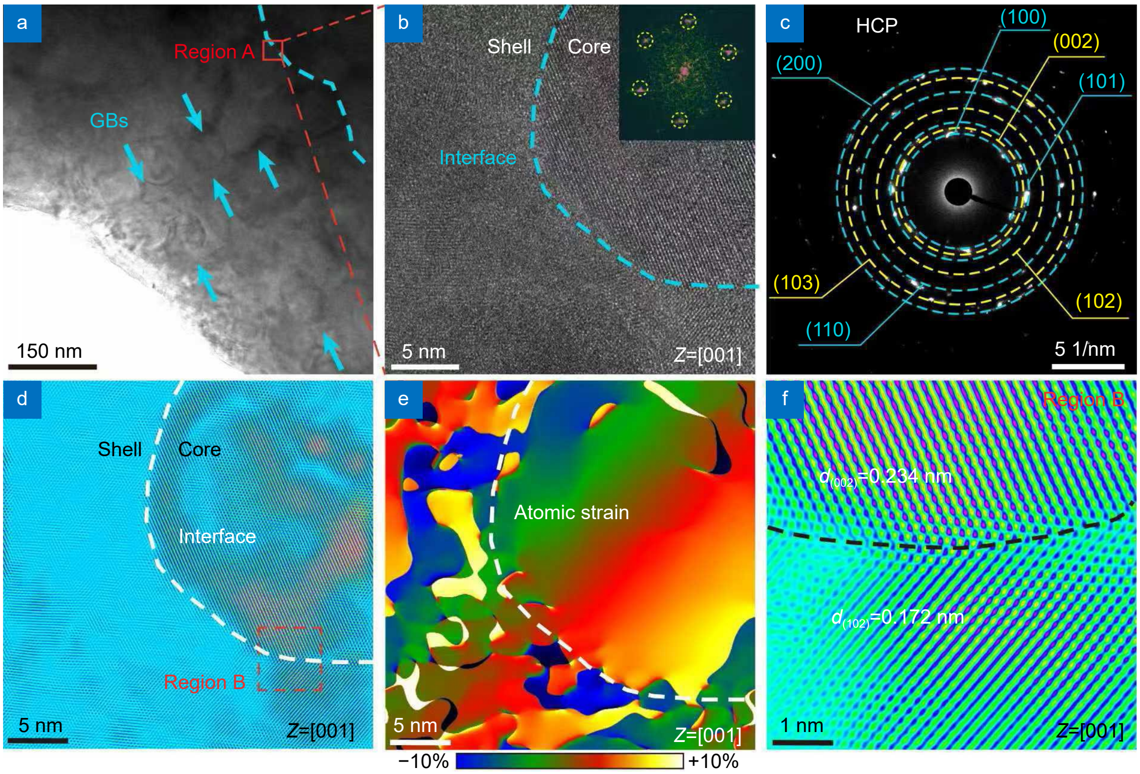

Fig. 3 | The core-shell heterostructure of MMed pure Ti powders: (**a**) TEM pattern, (**b**) HRTEM and FFT patterns, (**c**) SAED pattern, (**d**) lattice fringes under IFFT pattern and (**e**) the atomic strains from *Z* = [001] axis corresponding to region A, and (**f**) an enlarged IFFT pattern corresponding to region B.

adhesion of small-sized satellite particles, which was consistent with the EBSD results in Fig. 2(a). Compared to the initial Ti powders, MMed powders displayed a plastic deformation region with wrinkled structure introduced by intense collisions on the surface layer of particles, along with the disappearance of satellite powders (Fig. 4(b)). Furthermore, the deformation and roughness became ever-increasingly obvious with incremental MM-time (Fig. 4(b–d)). A similar phenomenon was also reported in other MMed powders[36,37] and attributed to the persistent and increasing energy input during MM process. It was noted that MM-10 and MM-20 powders

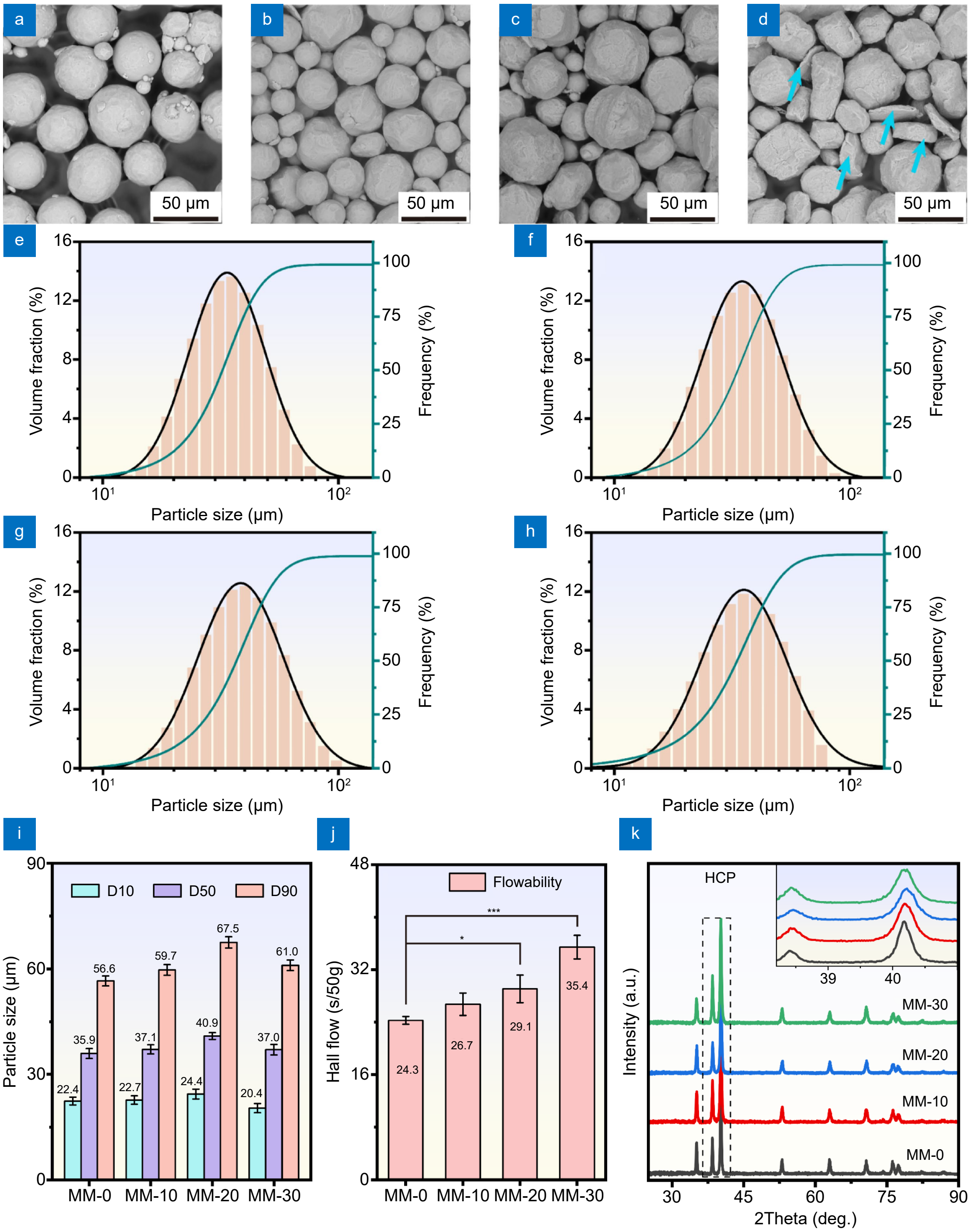

Fig. 4 | The morphology and microstructure evolutions of pure Ti powders with increasing MM-time: the SEM images of (**a**) MM-0, (**b**) MM-10, (**c**) MM-20 and (**d**) MM-30 powders, the PSD curves of (**e**) MM-0, (**f**) MM-10, (**g**) MM-20 and (**h**) MM-30 powders, (**i**) D10, D50 and D90 values, (**j**) powder flowability, and (**k**) XRD patterns.

showed a near-spherical morphology due to applicable energy inputs during MM process, which was essential to flowing, melting, and solidifying for LPBF process (Fig. 4(f–g)). Discrepantly, some flattened particles (blue arrows in Fig. 4(d)) were observed in MM-30 powders caused by excessive energy input, which might be adverse to the flowability and LPBF consolidation[17]. Moreover, the PSDs of Ti powders upon various MM-time were measured. As shown in Fig. 4(e–h), MMed Ti powders were similar in size to the initial powders, and the PSD curves of all powders displayed a monomodal Gaussian distribution. Specifically, with increasing MM-time (Fig. 4(i)), the D50 value increased from 35.9 μm (MM-0) to 40.9 μm (MM-20), while both the D10 and D90 values increased from 22.4 μm to 24.4 μm and from 56.6 μm to 67.5 μm, respectively. This result demonstrated a slight increase in the D10 value at the low end of the particle size range after MM treatment, thus substantiating the disappearance of satellite particles (< 10 μm) in Fig. 4(a–c). Inversely, it was noted that the D10, D50, and D90 values all decreased as MM-time reached 30 h, owing to the flattening and possible fracture of powders upon a prolonged collision.

More importantly, the Hall Flow was measured to quantificationally evaluate the flowability of MMed Ti powders (Fig. 4(j)). In this work, MMed Ti powders with flowability of 24.3~35.4 s/50 g were all similar to the reported powders for LPBF consolidation[35,38,39], which could be qualified for the subsequent LPBF consolidation. As known, powder flowability is regulated by PSD and morphology characteristics of the particles[38]. The decreasing size dispersity of powder will enhance overall flowability because the extra small particles within powder bed can decrease the specific surface area of powders and interparticle friction[40]. Hence, the central and narrow PSD of MMed powders in this study demonstrated appropriate flowability for LPBF consolidation of Ti implants. In addition, the flowability of MM-30 powders (35.4±1.8 s/50 g) was somewhat inferior to MM-0 powders (24.3±0.6 s/50 g). This was attributed to the increased interparticle friction induced by the partial flattened particles, and may affect the localized quality during LPBF consolidation.

Whereafter, the phase structures of MMed Ti powders were also investigated by XRD analysis (Fig. 4(k)). All the powders showed a single HCP structure with the same diffraction peaks and angles, which indicated full α grains without $\alpha \rightarrow \beta$ phase transformations in the final Ti powders after MM process. Moreover, the diffraction peaks presented a distinctly broadening phenomenon of full width at half maximum peaks with increasing MM-time, which qualitatively confirmed the grain refinement upon MM process. In conclusion, MM process not only preserved near-spherical morphology of powders, but also induced a gradient plastically deformed layer for constructing heterogeneous core-shell regions, which was an essential prerequisite for achieving heterostructure in pure Ti implants.

Heterostructure in the LPBF consolidated Ti implants

To evaluate the evolution of grain and dislocations during LPBF process, the microstructure features of LPBF fabricated Ti samples (HS-0, HS-10, HS-20, and HS-30) were characterized by EBSD on the transverse section perpendicular to the [0001] orientation. Notably, the building direction (BD) is parallel to the [0001] orientation. As known, the structure and feature of prior-β grains during high temperature can influence the α grains and final properties for pure Ti[41,42]. Hence, the prior-β grains were reconstructed from α grains by EBSD maps through the Burgers orientation relationship of $\{0001\}_\alpha$ // $\{101\}_\beta$ and $<11\text{-}20>_\alpha$ // $<111>_\beta$. As shown in Fig. 5, the changes in prior-β grains could be explicitly observed. In Fig. 5(a), HS-0 sample without MM pre-treatment displayed the coarse prior-β grains and a strong < 001 > crystal orientation with a maximum multiples random distribution (MRD) value of 9.67. Comparatively (Fig. 5(b)), after MM pre-treatment, HS-10 sample had more refined and equiaxed prior-β grains with smaller MRD value (5.27). Further, with increasing MM-time, the size and MRD values of prior-β grains decreased visibly in HS-20 and HS-30 samples. Yao et al.[42] reported that the refinement of prior-β grains may contribute to an increase in strength of Ti alloys. More importantly, the crystal orientation of α grains is determined by the MRD value of prior-β grains during the $\beta \rightarrow \alpha$ transformation according to Burgers orientation relationship. Therefore, the decrease in MRD values of prior-β grains was beneficial to weaken the formation of α grains textures during LPBF process, which could refrain from the anisotropy of properties.

As shown in IPF map (Fig. 6(a)), HS-0 sample displayed a homogeneous structure with CGs. In contrast, HS-10 sample emerged a peculiar microstructure wherein CGs (framed areas) were enclosed by UFGs (Fig. 6(b)),

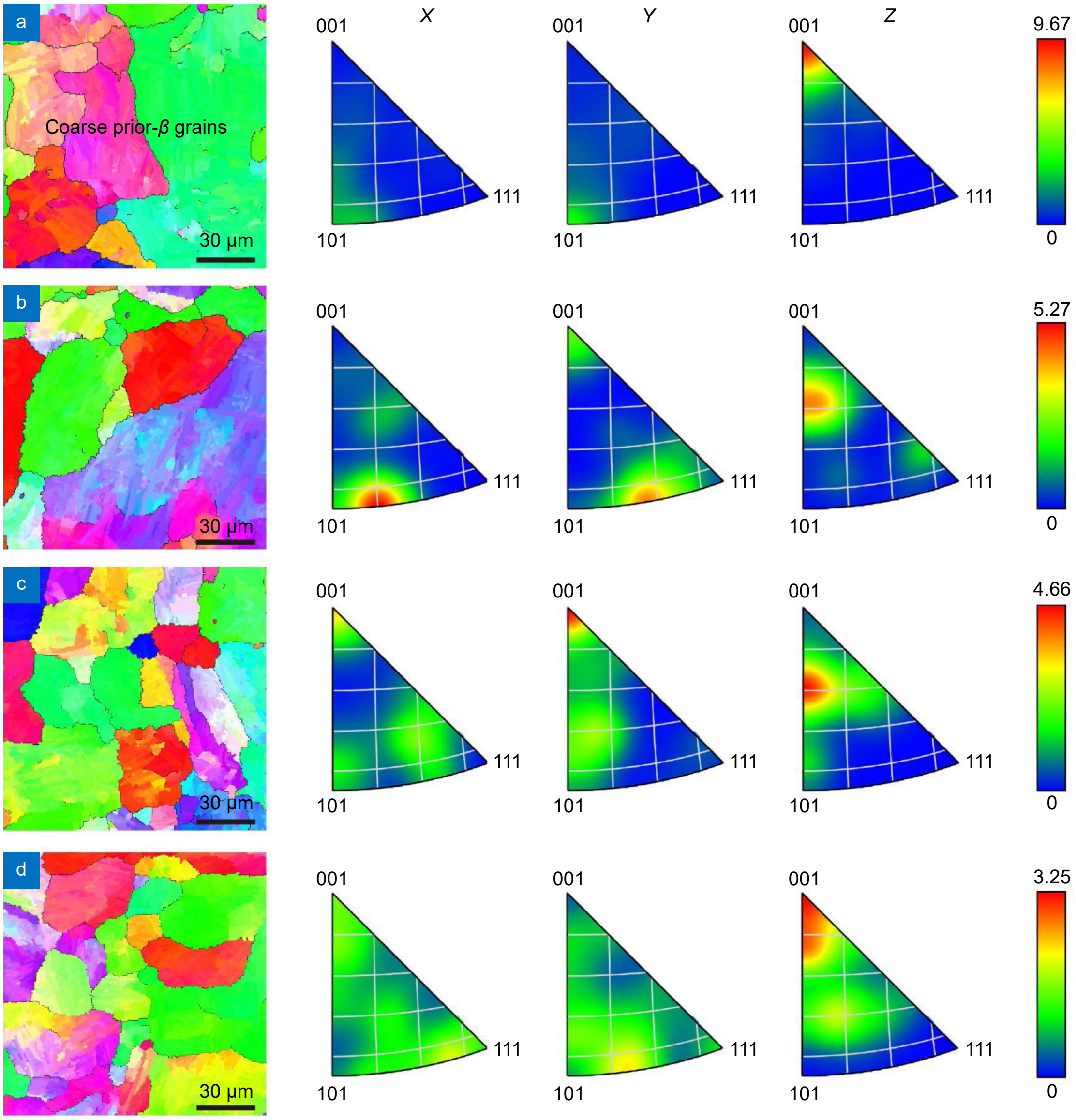

Fig. 5 | The prior-*β* grains reconstructed from the *α* grains of LPBFed Ti samples upon different MM pre-treatment: (**a**) HS-0, (**b**) HS-10, (**c**) HS-20, and (**d**) HS-30.

termed as a harmonic heterostructure. It should be noted that the black areas within the UFGed regions were suspected to be unidentifiable nano-grains due to the limitation of EBSD system[43]. With the prolonging MM-time up to 20 h and 30 h (Fig. 6(c, d)), the volume of UFGed shell regions increased gradually, leading to a more distinct difference in grain size between the core and shell regions. Compared with HS-10, a more prominent harmonic heterostructure was induced within HS-20 and HS-30 samples. These results suggested the successful preparation of heterostructured pure Ti consisting of CGs surrounded by UFGs, which was attributed to a feasible and adjustable route of MM and LPBF process. On the one hand, the highly transient-melting kinetics and localized nature during LPBF led to the interaction time between laser and powders being extremely short (10^{-6}–10^{-3} s[44,45]). This restrained the regrowth of initial UFGs constructed by MM due to the ultra-fast heating and cooling rate. On the other hand, the severe plastic deformations by MM pre-treatment triggered UFGs in Ti particles, accompanied by the residual nuclei and pre-existing dislocations in UFGed shell regions. These residual nuclei provided growth sites for partial primary grains, and pre-existing dislocations supplied the driving force for the formation of extra UFGs within Ti samples[46]. Hence, the initial grain size heterogeneity (core-shell) formed by MM pre-treatment was successfully carried over to LPBFed Ti samples, thereby establishing a

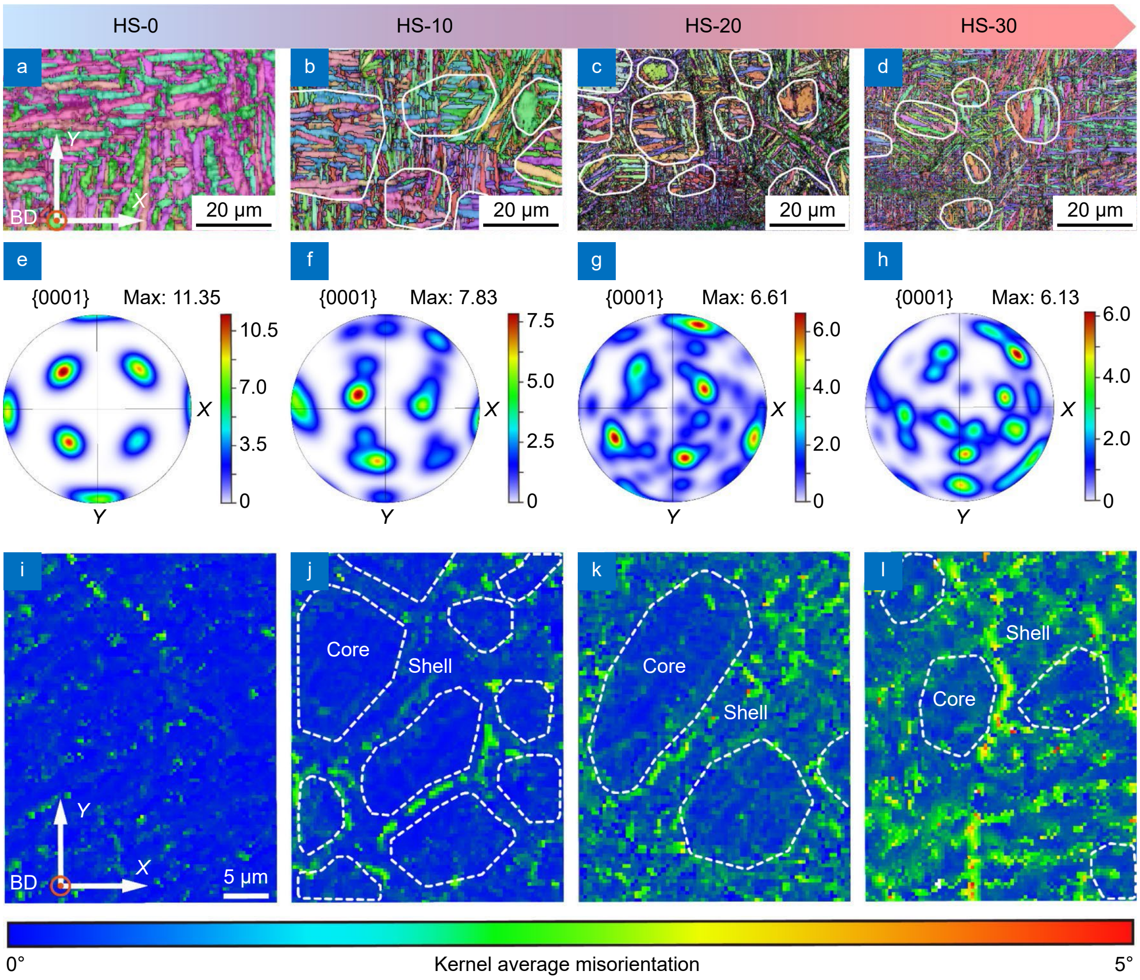

Fig. 6 | The microstructure evolution of LPBFed Ti samples upon different MM pre-treatment: (**a**–**d**) IPF, (**e**–**h**) PF, and (**i**–**l**) KAM maps.

harmonic heterostructure with CGs surrounded by interconnected UFGs. Furthermore, the volume of core-shell regions was highly tunable owing to the configurable nature of MM pre-treatment.

Afterwards, combined with the summarized PF maps in Fig. 6(e–h), the harmonic heterostructured Ti samples (HS-10, HS-20, and HS-30) had smaller MRD values (7.83, 6.61, and 6.13, respectively) compared to the HS-0 sample (11.35). This suggested that the UFGs of heterostructure could improve the microstructure isotropy. As reported by Mandal et al.[47], the smaller initial grain sizes could weaken the formation of textures during the extremely rapid cooling rates, thereby eliminating the anisotropy of materials. This was due to the formed α grains during the $\beta \rightarrow \alpha$ transformation also inherited the crystal orientation of prior-β grains following the Burgers orientation relationship. Also, eliminating the textures of α grain was key to elevating plasticity of LPBFed Ti alloys.

Visually, the dislocation density evolution within LPBFed pure Ti upon different MM pre-treatment was further characterized by the KAM patterns from EBSD orientation data. As previously mentioned, the heterogeneous regions could be estimated by the dislocation density distributions. As shown in Fig. 6(i), the KAM pattern of HS-0 sample without MM pre-treatment displayed a thoroughly low dislocation density with plentiful blue regions. In comparison, a drastic variation in KAM values could be observed in the heterogeneous Ti samples (HS-10, HS-20, and HS-30) with MM pre-treatment, which was related to grain refinement since misorientations were concentrated near the GBs[26,48]. In Fig. 6(j), the LPBFed HS-10 sample was dominated by high dislocation density and emerged a harmonic distribution composed of low dislocation density in core regions and high dislocation density in shell regions, further presenting a harmonic heterostructure within the LPBF sample. Furthermore, as MM-time progressed (Fig. 6(j–l)), everincreasing pre-existing dislocations were introduced into the shell regions, which rendered a more pronounced harmonic structure. In addition, dislocation density is widely used to evaluate the mechanical performance of metals[46,49], and the higher dislocation density in the present study suggested significant mechanical heterogeneity within the heterostructured Ti. In conclusion, the highly transient-melting kinetics and localized nature of LPBF process effectively perpetuated the grain heterogeneity induced by MM pre-treatment, hence establishing a harmonic heterostructure within consolidated pure Ti implants. Furthermore, the pre-existing dislocations in the heterostructured Ti implants were believed to contribute to the following mechanical properties.

Strength and plasticity

Mechanical properties are crucial for orthopedic implants, especially for internal support and organ replacements. Hence, strength, plasticity and wear resistance are considered to be the most momentous performances for clinical applications. To further shed light on the harmonic heterostructure for strength and plasticity, tensile tests were carried out on the LPBF fabricated Ti samples with different MM pre-treatment. The engineering stress-strain curves of homogeneous and heterogeneous Ti samples were displayed in Fig. 7(a). For HS-0 sample, the ultimate tensile strength and elongation were 594.2±12.1 MPa and 9.8±0.2%, respectively. Comparatively, HS-10 sample exhibited a simultaneously improved strength (875.7±21.6 MPa) and plasticity (13.1±0.3%). This phenomenon suggested that the harmonic heterostructure within the Ti samples contributed to the synergistic enhancement of strength and plasticity. Furthermore, mechanical properties of pure Ti samples increased prominently owing to the construction of harmonic heterostructure, which was adequately confirmed by the statistical analysis results in Fig. S3. Particularly, HS-20 sample possessed the best combination of strength (989.2±22.3 MPa) and plasticity (15.3±0.4%) which were 60% and 38% higher than those of HS-0 sample, respectively. Nonetheless, the increase of strength (1084.1±28.1 MPa) in HS-30 sample was accompanied with a decrease of plasticity (11.6±0.5%) compared to HS-20 sample. This trade-off phenomenon might be on account of the superfluous refined grains and reduced powder flowability during LPBF process, as reported by ref.[50,51]. The slightly inferior flowability of MM-30 powders led to uneven layer thickness, with excessive and insufficient energy input in thinner and thicker regions, respectively. As a result, compared to HS-0, HS-10, and HS-20 samples (Fig. S4(a–c)), the thermodynamics and kinetics differences in powder-layers generated the localized concentration of residual stress during cooling and solidification, inducing various internal micro-cracks and voids in HS-30 sample (Fig. S4(d)).

These results demonstrated that the introduction of heterogeneous regions produced a positive effect on the strength and plasticity of pure Ti samples, which may be associated with hetero-deformation in harmonic heterostructure. Especially, the manipulation of core-shell volumes by utilizing the nature of MM and LPBF process induced an excellent synergistic effect on strength and plasticity within HS-20 sample. In addition, it is well known that the strength-plasticity is also determined by strain-hardening rate (SHR: Θ) defined as:

$$\Theta=\partial\sigma_T/\partial\varepsilon_T, \tag{4}$$

in which σ_T and ε_T are true stress and true strain, respectively. The intersection between Θ and σ_T corresponds to plastic instability points, after which necking occurs[28]. A comparison of SHR and true stress as a function of true strain was shown in Fig. 7(b). Interestingly, the SHRs of Ti samples were substantially enhanced, benefiting from the harmonic heterostructure, and thereby the point of plastic instability was successfully postponed, leading to improved strength and plasticity. Especially, HS-20 sample exhibited the optimal strain-hardening capability. Therefore, it could be deduced that a superior strain-hardening capacity of heterostructure delayed the plasticity instability, thereby achieving a synergistic high strength and plasticity in LPBFed pure Ti, which contributed to the long-term service as orthopedic implants.

Thereafter, the fracture topographies of LPBFed Ti samples were characterized by SEM to visualize the fracture patterns. As shown in Fig. 7(c), HS-0 sample exhibited a fracture pattern dominated by certain cleavage and river-like topographies, accompanied by a few shallow dimples. Furthermore, as the volumes of UFGed shell regions increased (Fig. 7(d, e)), the fracture topographies exhibited a notable evolution of discernible necking phenomenon and deep dimples, similar to a study by Cui et al.[52]. Also, HS-20 sample presented the most abundant dimples with sizes less than 20 μm, suggesting a strong intergranular bonding between the core and shell regions, which contributed to the promotion of mechanical stability[53]. Consequently, the mechanical performance of

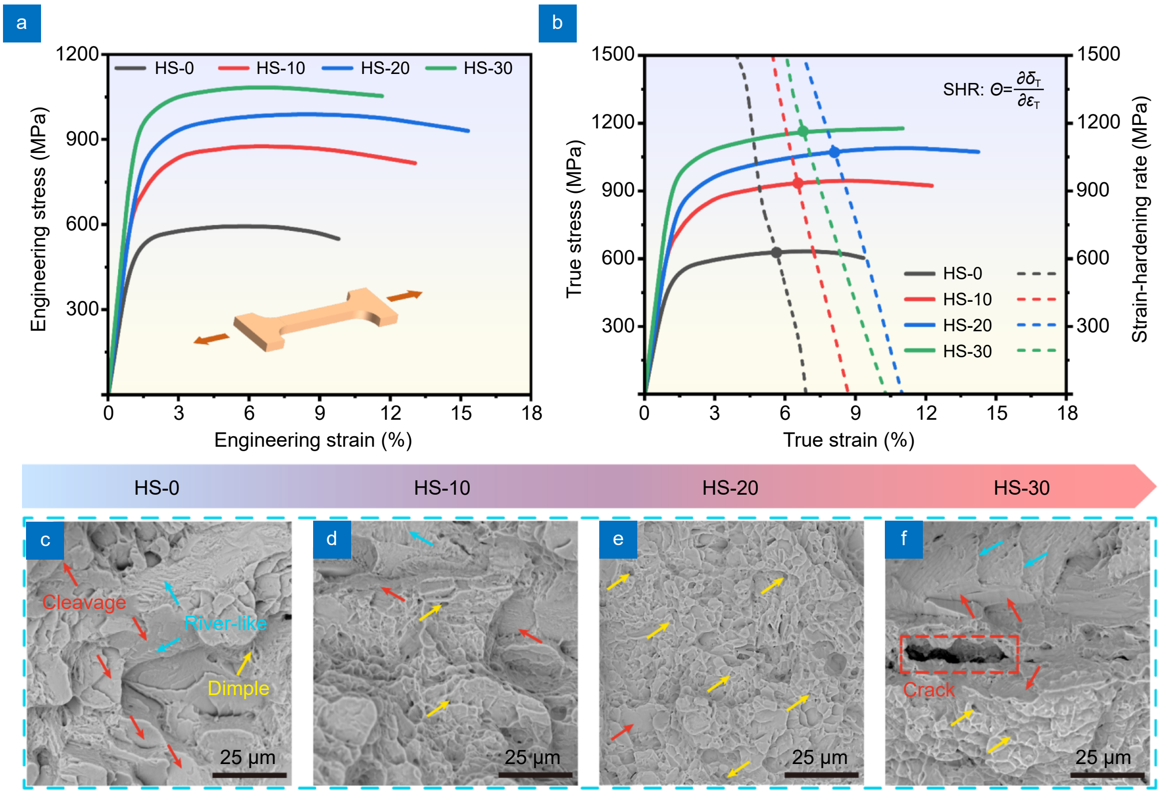

Fig. 7 | The mechanical properties of LPBFed Ti samples upon different MM pre-treatment: (**a**) engineering stress-strain curves, (**b**) true stress-strain curves, and (**c**–**f**) SEM images of fracture surface morphologies.

HS-20 sample transitioned from mixed fracture to ductile fracture predominated by the abundant dimples. Comparatively, HS-30 sample showcased the growth and development of intergranular cracks, as well as stress concentration during deformation, which was attributed to the superfluous UFGs and inferior consolidation quality. In conclusion, the Ti implants in the present study achieved a remarkable strength-plasticity synergy owing to the harmonic heterostructure and superior strain-hardening capacity.

Wear resistance

To evaluate wear resistance of the heterostructured Ti implants in this study, the frictional behaviour and microhardness were investigated via friction and indentation tests. The variations in COFs as a function of time for the homogeneous and heterostructured Ti samples were presented in detail under varying friction pairs and loads, respectively. As shown in Fig. 8(a), the frictional behaviour reached a steady state after running ~1300 s, with a Si_3N_4 friction pair and a constant load of 5 N, which suggested a COF of 0.58 for homogeneous HS-0 counterpart. For heterostructured HS-10, HS-20 and HS-30 samples, the corresponding COFs presented an evolution trend, i.e., first decreasing from 0.52 to 0.42 followed by increasing to 0.53. This result manifested that HS-20 sample possessed the minimum COF, and then the frictional behaviour of HS-20 sample was further explored under varying loads of 2.5, 5, 7.5 and 10 N, respectively. As shown in Fig. 8(b), the COFs kept no apparent change, suggesting an analogous frictional behaviour of Ti samples under the varying loads. In addition, UHMWPE balls as friction pairs were employed to investigate the frictional behaviour under different working conditions (Fig. 8(c)). The COFs of all samples tended to stabilize earlier than that measured using Si_3N_4 balls, as well as notably lower COFs (0.11–0.17), which suggested the obvious mechanical stability. As known, the implant would be situated in a stable environment of human body and hardly subjected to additional loads after implantation[54]. Furthermore, Ti is an easily passivated metal, which promotes the formation of extremely dense, stable, and chemically inert protection film[55–57]. In this work, the UFGs of heterostructure with more GBs provided a higher number of active atoms for passivation, which further enhanced the corrosion resistance of

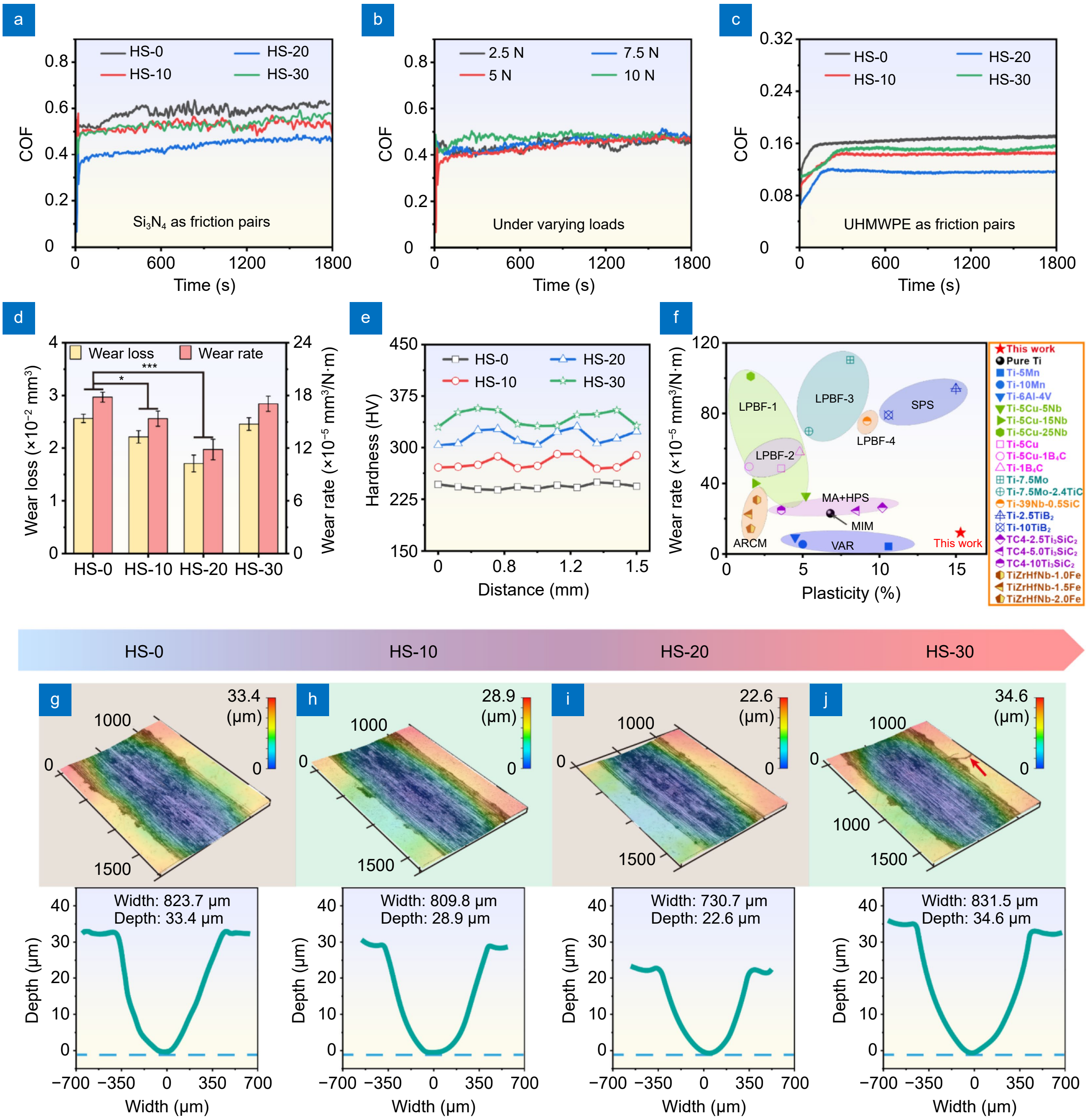

Fig. 8 | The frictional behaviour of LPBFed Ti samples upon different MM pre-treatment: COFs of (**a**) Si_3N_4 as friction pairs under a constant load of 5 N, (**b**) Si_3N_4 as friction pairs under varying loads of 2.5, 5, 7.5 and 10 N, (**c**) UHMWPE as friction pairs under a constant load of 5 N, respectively, (**d**) wear loss and rate with Si_3N_4 as friction pairs under constant load of 5 N, (**e**) microhardness, (**f**) plasticity and wear resistance profiles of the reported Ti-based alloys, and (**g**–**j**) microscopic morphologies and corresponding depth-width curves of wear-scars. Annotation: MIM with sintering of 1250 °C for 2 hours, VAR with remelting of 1780 °C, LPBF-1 with *E* of 186 J/mm³, LPBF-2 with *E* of 125 J/mm³, LPBF-3 with *E* of 87 J/mm³, LPBF-4 with *E* of 111 J/mm³, SPS with sintering of 1050 °C for 5 minutes, and MA+HPS with sintering of 1200 °C for 1 hour.

heterostructured Ti implants. More importantly, after surgical implantation, cells adhering to Ti implant surface would form direct structural and functional connection between the implants and bone tissues, which provided biomechanical support for the orthopedic implants[5,58,59]. Therefore, the heterostructured Ti orthopedic implants in this work are expected to maintain stability under joint friction and thereby serve as potential applications for long-term service.

To further explore the wear resistance, wear loss of all Ti samples with Si_3N_4 balls and constant load of 5 N was measured and shown in Fig. 8(d). The evolution trend of wear loss was similar to that of COFs, further confirming quantificationally that wear resistance of harmonic heterostructured Ti samples was higher than that of homogeneous counterpart. Further, the wear rate (ω) was calculated based on wear loss according to the equation[3]:

$$\omega = V_{\text{loss}}/(F\times L), \tag{5}$$

where ω is a wear rate (mm^3/Nm), V_{loss} is a wear volume loss (mm^3), F is an applied load (N) and L is a sliding distance (m). Particularly, heterostructured HS-20 sample exhibited the minimum wear rate ($11.8\pm1.2\times10^{-5}$ mm^3/Nm) which was reduced by 33.7% compared to homogeneous HS-0 counterpart ($17.8\pm0.6\times10^{-5}$ mm^3/Nm), suggesting the optimal wear resistance. In addition, microhardness is also known as one of the factors for wear resistance[55]. As the volume of UFGed shell regions increased (Fig. 8(e) and Fig. S3), the mean microhardness of Ti samples presented a significant increasing trend (243.5±3.4, 278.1±9.1, 315.8±10.3, and 343.4±10.9 HV, respectively). It is well known that grain refinement leads to increased microhardness of metals[58], which may be responsible for the higher microhardness in the present study. Moreover, a diagram (Fig. 8(f)) compared the plasticity and wear resistance of LPBFed Ti implants in this work with those of reported Ti-based alloys by other processes, including metal injection molding (MIM)[3], vacuum arc remelting (VAR)[61], LPBF[4,62–64], spark plasma sintering (SPS)[65], mechanical alloying (MA) and subsequent hot-pressing sintering (MA+HPS)[66], arc-melting (ARCM)[67]. As known, the sacrificed plasticity owing to enhanced strength will deprive the capability to absorb energy and repeat deformations during friction, which is detrimental to mechanical stability and wear resistance. Fortunately, the harmonic heterostructured Ti in this work stood out in comparison to the reported alloys, exhibiting a marvelous synergy of wear resistance and plasticity.

Intuitively, the wear surface morphologies and corresponding sectional curves were shown in Fig. 8(g–j), displaying the variations in depth and width of wear-scars. From the macroscopic view (Fig. 8(g)), the wear surface was characterized by abundant grooves and irregular boundaries, suggesting that HS-0 sample suffered severe wear. Comparatively, upon MM pre-treatment (Fig. 8(h–j)), the heterostructured Ti samples displayed shallow and narrow wear-scars with fewer grooves, as well as more orderly boundaries, and this phenomenon was ever-increasingly obvious with the increasing volume of UFGed regions. It was worth noting that HS-20 sample presented the minimum depth and width of the wear-scars, confirming the maximum reinforcement effect owing to heterostructure. In addition, an obvious crack (red arrow) appeared on the wear surface of HS-30 sample, which was attributed to the insufficient plastic deformation capacity during frictions. Hence, the harmonic heterostructured Ti samples displayed a significant spatial difference between the soft core and hard shell compared to homogeneous counterparts, thereby leading to enhanced wear resistance. In brief, an excellent wear resistance was achieved via constructing harmonic heterostructure in pure Ti implants, and reinforcing mechanisms would be concretely explored in the following sections.

Reinforcing mechanisms

To elucidate the correlation between harmonic heterostructure and exceptional mechanical properties, a systematic analysis was conducted on the heterogeneous grains and dislocation behaviours within LPBFed Ti samples through TEM characterization. As shown in Fig. 9(a), obvious heterogeneous grains of CGs encased by UFGs were marked in detail. More specifically, pre-existing dislocations (blue arrows) piled up at the heterogeneous interfaces. Further, the SAED pattern (Fig. 9(b)) of marked grains further suggested pure Ti samples with the representative lattice planes of the HCP structure. The corresponding EDS mapping (Fig. 9(c)) manifested pure Ti samples without other elements, and the SAED pattern of single crystal (Fig. 9(d)) presented a lattice parameter of c/a=1.586. The corresponding HRTEM pattern indicated HCP structure at the atomic level projected along the [110] direction. These results convincingly verified that heterostructured Ti samples possessed a single HCP structure illustrated in Fig. 9(e). Moreover, a distinct interface between the core and shell regions, and the specific lattice fringes with heterogeneous interfaces were identified in enlarged (Fig. 9(f)) and IFFT (Fig. 9(i)) patterns, respectively. This was attributed to the discrepancies in the orientation of lattice fringes between core and shell regions. The interplanar spacing within core and shell regions were 0.234 nm and 0.224 nm, respectively, which was congruent with the typical structure of pure Ti.

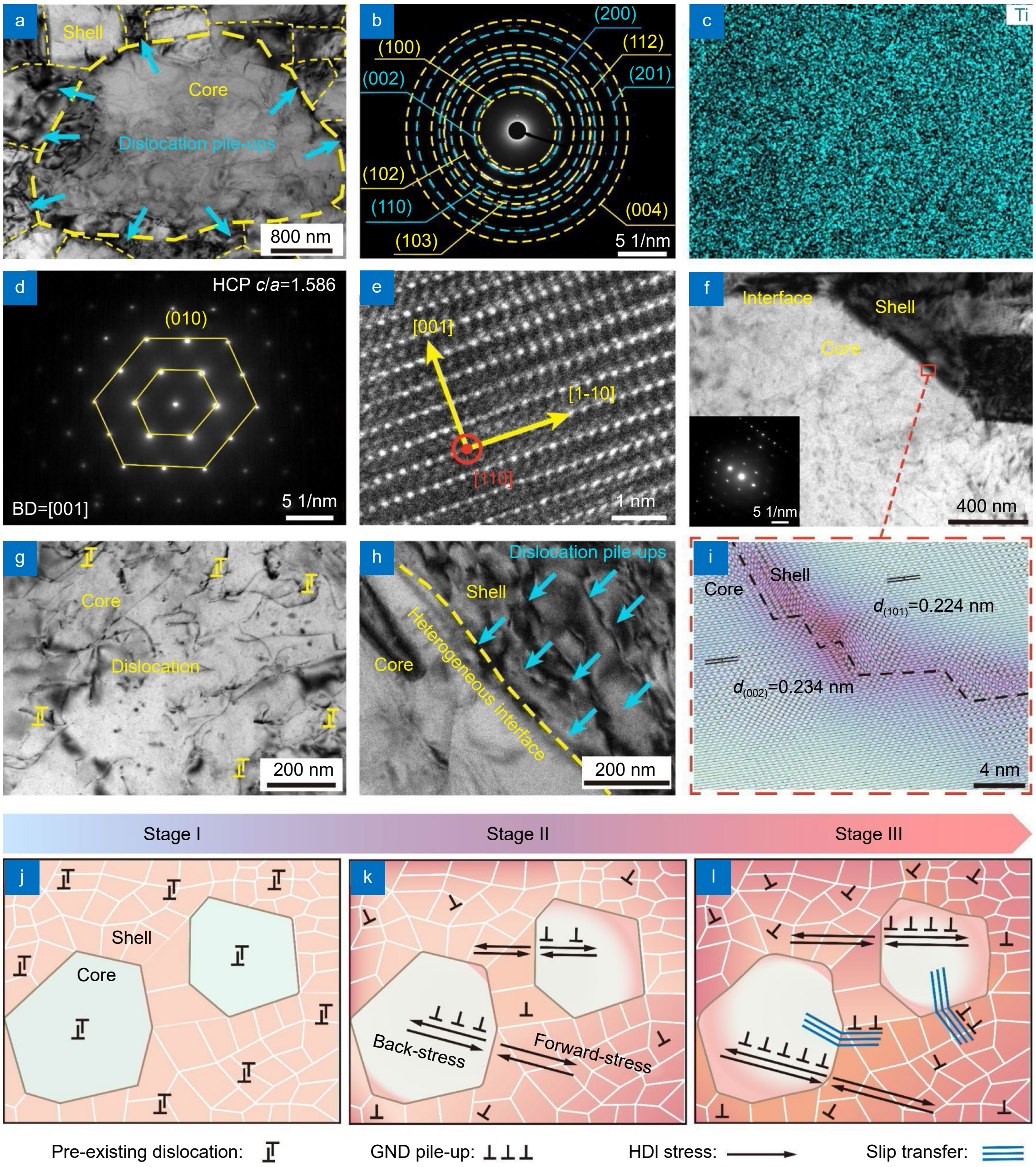

Fig. 9 | The microstructure characterizations of heterostructured Ti samples: (**a**) TEM image of heterostructure distribution, the corresponding (**b**) SAED pattern, (**c**) EDS mapping, (**d**) SAED pattern of single crystal and (**e**) HRTEM pattern of (a), (**f**) core-shell heterogeneous interfaces, (**g**) dislocation distribution in core regions, (**h**) pre-existing dislocation pile-ups at heterogeneous interfaces, (**i**) corresponding IFFT pattern of core-shell regions, and (**j–l**) schematic illustration of deformation mechanism.

Further, more obvious evidences demonstrated the disparate dislocation distributions between the core and shell regions. In Fig. 9(g), dislocations were diffusely distributed inside the CGs. In contrast, in the UFGs induced by MM pre-treatment, abundant dislocations were entangled with each other, leading to significant pre-existing dislocation pile-ups (Fig. 9(h)). These results indicated that the strong plastic deformation produced by MM pre-treatment contributed to massive dislocation pile-ups in UFGed shell. These pre-existing dislocation pile-ups within the heterogeneous regions were conducive to synergistic strength-plasticity.

Intuitively, a possible schematic diagram was proposed and illustrated in Fig. 9(j–l) to reveal the strength-plasticity synergy of the harmonic heterostructured Ti samples. At the initial stage of deformation (Fig. 9(j)), the pre-existing dislocation pile-ups within UFGed shell impeded dislocation motions, thus contributing to more strength for shell regions. Moreover, the enhancement in mechanical stability was ascribed to the pre-existing dislocations, where dislocations could act as barriers for the deformation of CGs. At this period, the soft core was still at the plastic deformation stage, which was attributed to the surrounding hard shell[68]. Therefore, the mechanical incompatibility between the shell and core regions of LPBFed Ti samples introduced significant gradient strain near the heterogeneous interfaces.

With strain increasing (the second stage in Fig. 9(k)), geometrically necessary dislocations (GND) in core regions during hetero-deformation were activated and began to pile up near the heterogeneous interfaces of pure Ti. Subsequently, the continuous and accumulated GND triggered hetero-deformation induced (HDI) stress, including back-stress in core and forward-stress in shell. The forward-stress motivated the pre-existing dislocations in shell to reverse or cross slip along slip planes, which led to the disentanglement and annihilation of dislocations. This was a typical strain-softening effect that freed up space in shell, enabling the regeneration and storage of dislocations in pure Ti. Afterwards, early strain localization was postponed, allowing for further plastic deformation of UFGs[69,70]. Meanwhile, the back-stress led to HDI strengthening of CGed core, further eliminating strain localization of heterostructured Ti implants.

At a critical threshold of the back-stress (the third stage in Fig. 9(l)), dislocation behaviours including multiple slips and slip transfer across heterogeneous interfaces were activated in the LPBFed Ti samples. It was emphasized that the dislocation behaviours benefited from the gradient grain structure and good interfacial compatibility between heterogeneous regions. Hence, in addition to the above two dislocation behaviours, abundant $<c+a>$ slips were also activated near the heterogeneous interfaces. Ultimately, the HDI stress triggered the extra strain-hardening in pure Ti, defined as HDI hardening (Θ_{HDI}), which could be mathematically expressed as[71]:

$$\Theta_{\mathrm{HDI}} = -(\partial\sigma/\partial\varepsilon)_{\mathrm{SS}} + (\partial\sigma/\partial\varepsilon)_{\mathrm{UFG}} + (\partial\sigma/\partial\varepsilon)_{\mathrm{CG}}, \qquad (6)$$

where $-(\partial\sigma/\partial\varepsilon)_{\mathrm{SS}}$ was the initial strain-softening in UFGs, and $(\partial\sigma/\partial\varepsilon)_{\mathrm{UFG}}$ and $(\partial\sigma/\partial\varepsilon)_{\mathrm{CG}}$ were HDI hardening in UFGs and CGs, respectively. At this stage, the HDI hardening effect in the UFGs was much stronger than the initial strain-softening, along with the HDI hardening in CGs, thus endowing the Ti samples with a significant HDI hardening effect. In brief, these pre-existing dislocations and heterogeneous grain structures induced strain-softening, HDI strengthening and HDI hardening, which contributed to the enhanced strength and strain-hardening rate and eventually unprecedented strength-plasticity synergy.

Furthermore, the reinforcing mechanisms of heterostructure for wear resistance were revealed through TEM characterization of pure Ti implants after wear tests. A HAADF image of wear-scar section was shown in Fig. 10(a), and the enlarged image of Fig. 10(b) suggested that pure Ti samples still maintained the heterostructure of CGed core encased by UFGed shell. As shown in Fig. 10(c), more extensive GND tended to pile up within CGs due to repeated shear-stress during friction deformation. Further, the GND pile-ups with the identical Burger's vector contributed to the formation of dislocation walls at heterogeneous interfaces[72]. As displayed in Fig. 10(d), an enlarged image of heterogeneous interfaces indicated discrepant regions (yellow dotted line). As confirmed by HRTEM image and inset FFT pattern in Fig. 10(e), heterostructured Ti samples possessed a typical (102) crystalline plane with lattice spacing of 0.172 nm. In Fig. 10(f), a IFFT pattern of region C further demonstrated that the high density of GND was observed at the heterogeneous interfaces, suggesting the outstanding dislocation storage capability of heterostructure during friction deformation.

A schematic illustration of friction revealed the microstructure evolution of heterostructured Ti during friction deformation. As shown in Fig. 10(g, h), the high strength of UFGed shell could bear wear shear-stress and effectively protect CGed core from premature deformations, while the abundant GBs and pre-existing dislocations also effectively impeded material removal from Ti samples. Meanwhile, the HDI hardening induced by GND pile-ups enhanced strain-hardening capacity during the repeated shear sliding, thus hindering the generation and expansion of cracks[73]. More importantly (Fig. 10(i)), the GND pile-ups at heterogeneous interfaces contributed to the formation of dislocation walls, which induced back-stress at the interfaces between CGed core and UFGed shell. The back-stress as a long-range internal stress was in the opposite direction to the applied stress of wear and could offset part of wear shear-stress, which endowed the heterostructure with shear-resistance, thus

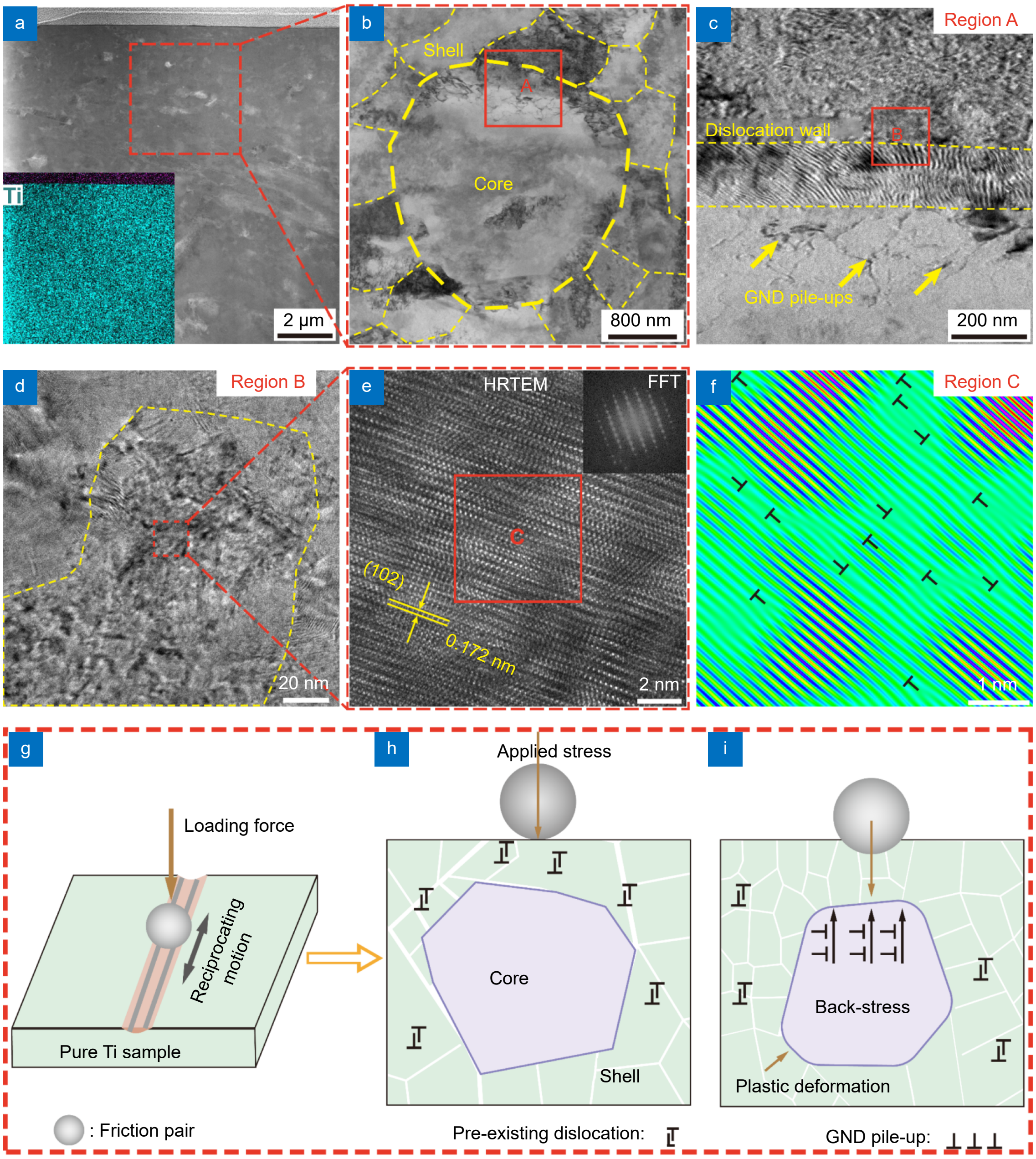

Fig. 10 | The microstructure evolution of heterostructured Ti samples after wear testing: (**a**) HAADF image of wear-scar section with corresponding EDS mapping, (**b**) TEM image of heterostructure feature, (**c**) enlarged region A in (b), (**d**) dislocation structure of region B in (c), (**e**) HRTEM image of the region marked in (d) with corresponding FFT pattern, (**f**) corresponding IFFT pattern of region C in (e), and (**g–i**) schematic illustration of wear behaviour.

postponing plastic deformation and cracking. The soft core regions possessed plasticity to relieve stress concentration, and the hard shell regions also absorbed part of the stress. Therefore, HDI strengthening and hardening, and back-stress collaboratively broke through the dilemma of strength-plasticity trade-off, contributing to the outstanding wear resistance in LPBF fabricated pure Ti implants.

Conclusions

In the present work, harmonic heterostructured pure Ti implants were developed by a combined route of MM and LPBF technology to achieve synergistic strength-plasticity and outstanding wear resistance. The microstructure, dislocation behaviours, mechanical properties, and relevant reinforcing mechanisms were explored in detail. The main conclusions were as follows:

(1) During MM process, a spatial heterostructure of

UFGed shell encapsulating CGed core within pure Ti particles was constructed by the gradient and intense plastic deformation, accompanied by the generation of pre-existing dislocations. Moreover, the shell thickness and grain size distributions were highly tunable by manipulating the energy input of MM process.

(2) The subsequent LPBF process perpetuated initial grain heterogeneity due to highly transient-melting kinetics, hence creating a harmonic heterostructure within pure Ti implants. Furthermore, the pre-existing dislocations piled up near the heterogeneous interfaces within the heterostructured Ti implants.

(3) The harmonic heterostructured pure Ti implants exhibited an enhanced wear resistance (33.7%) compared to the homogeneous counterpart, which was ascribed to the synergistic strength-plasticity motivated by HDI strengthening and extra HDI hardening. Furthermore, the back-stress during the deformation counteracted the partial wear shear-stress, further contributing to the enhanced wear resistance.

These findings demonstrated the untapped potential of enlightening MM and LPBF strategy to develop heterostructure and further manipulate structural heterogeneity, which provided novel insights into breaking through wear resistance dilemma and manufacturing high-performance biomedical implants. The heterostructured pure Ti implants presented a marvelous synergy of strength-plasticity and wear resistance, which was attractive for orthopedic implant applications. Nevertheless, more further studies and validations are necessary for different biomedical application scenarios in future. In addition, adaptative elastic modulus between Ti implants and implantation sites is crucial to alleviate stress-shielding effect, which may also be the emphasis for future studies.

References

1. Zhao ST, Zhang RP, Yu Q et al. Cryoforged nanotwinned titanium with ultrahigh strength and ductility. *Science* **373**, 1363–1368 (2021).
2. Zhang TL, Huang ZH, Yang T et al. In situ design of advanced titanium alloy with concentration modulations by additive manufacturing. *Science* **374**, 478–482 (2021).
3. Zhou XX, Yuan TC, Xu YB. Complex-shaped titanium components fabricated via metal injection molding using hydride-dehydride titanium powder. *J Manuf Processes* **126**, 220–229 (2024).
4. Shi QM, Yang SF, Sun Y et al. *In-situ* formation of Ti-Mo biomaterials by selective laser melting of Ti/Mo and Ti/Mo_2C powder mixtures: a comparative study on microstructure, mechanical and wear performance, and thermal mechanisms. *J Mater Sci Technol* **115**, 81–96 (2022).
5. Wang RH, Wang MS, Jin RR et al. High strength titanium with fibrous grain for advanced bone regeneration. *Adv Sci* **10**, 2207698 (2023).
6. Zhou L, Liu G, Han Z et al. Grain size effect on wear resistance of a nanostructured AISI52100 steel. *Scr Mater* **58**, 445–448 (2008).
7. Zhu YT, Wu XL. Heterostructured materials. *Prog Mater Sci* **131**, 101019 (2023).
8. Gu L, Zhao YH, Li Y et al. Ultrastrong and ductile medium-entropy alloys via hierarchical ordering. *Sci Adv* **10**, eadn7553 (2024).
9. Xie YM, Meng XC, Chang YX et al. Heteroatom modification enhances corrosion durability in high-mechanical-performance graphene-reinforced aluminum matrix composites. *Adv Sci* **9**, 2104464 (2022).
10. Wu SW, Wang G, Wang Q et al. Enhancement of strength-ductility trade-off in a high-entropy alloy through a heterogeneous structure. *Acta Mater* **165**, 444–458 (2019).
11. Osaki K, Kikuchi S, Nakai Y et al. The effects of thermo-mechanical processing on fatigue crack propagation in commercially pure titanium with a harmonic structure. *Mater Sci Eng A* **773**, 138892 (2020).
12. Li X, Sun BH, Guan B et al. Elucidating the effect of gradient structure on strengthening mechanisms and fatigue behavior of pure titanium. *Int J Fatigue* **146**, 106142 (2021).
13. Darling KA, Rajagopalan M, Komarasamy M et al. Extreme creep resistance in a microstructurally stable nanocrystalline alloy. *Nature* **537**, 378–381 (2016).
14. Cao CZ, Yao GC, Jiang L et al. Bulk ultrafine grained/nanocrystalline metals via slow cooling. *Sci Adv* **5**, eaaw2398 (2019).
15. Wang ZM, Dong XL, Li XF et al. A contact-electro-catalysis process for producing reactive oxygen species by ball milling of triboelectric materials. *Nat Commun* **15**, 757 (2024).
16. Parsons EM, Shaik SZ. Additive manufacturing of aluminum metal matrix composites: mechanical alloying of composite powders and single track consolidation with laser powder bed fusion. *Addit Manuf* **50**, 102450 (2022).
17. Li GD, Jiang JX, Ma HC et al. Superior strength-ductility synergy in three-dimensional heterogeneous-nanostructured metals. *Acta Mater* **256**, 119143 (2023).
18. Cheng JQ, Liu P, Peng T et al. Mechanically alloyed $NiTiO_3$/transition metal heterostructures: introducing oxygen vacancies for exceptionally enhanced hydrogen evolution reaction activity. *J Mater Chem A* **8**, 14908–14914 (2020).
19. Suryanarayana C. Mechanical alloying: a critical review. *Mater Res Lett* **10**, 619–647 (2022).
20. Yao LY, Gao YM, Li YF et al. Preparation of nanostructural oxide dispersion strengthened (ODS) Mo alloy by mechanical alloying and spark plasma sintering, and its characterization. *Int J Refract Met Hard Mater* **105**, 105822 (2022).
21. Wang DW, Han HL, Sa B et al. A review and a statistical analysis of porosity in metals additively manufactured by laser powder bed fusion. *Opto-Electron Adv* **5**, 210058 (2022).
22. Ren J, Zhang Y, Zhao DX et al. Strong yet ductile nanolamellar high-entropy alloys by additive manufacturing. *Nature* **608**, 62–68 (2022).
23. Tan CL, Liu YC, Weng F et al. Additive manufacturing of voxelized heterostructured materials with hierarchical phases. *Addit Manuf* **54**, 102775 (2022).

24. Zhou KX, Cui DC, Chai ZS et al. In-situ tailoring microstructures to promote strength-ductility synergy in laser powder bed fusion of NiCoCr medium-entropy alloy. *Addit Manuf* **66**, 103443 (2023).
25. Jung HY, Choi SJ, Prashanth KG et al. Fabrication of Fe-based bulk metallic glass by selective laser melting: a parameter study. *Mater Des* **86**, 703–708 (2015).
26. Li B, Zhang W, Shen JC et al. Micro-laminated CoCrFeMnNi-TiNp/CoCrFeMnNi high-entropy alloy matrix composite with bimodal grain structure via multi-material selective laser melting (MM-SLM) additive manufacturing. *Compos Commun* **36**, 101366 (2022).
27. Munir KS, Li YC, Qian M et al. Identifying and understanding the effect of milling energy on the synthesis of carbon nanotubes reinforced titanium metal matrix composites. *Carbon* **99**, 384–397 (2016).
28. Chen JJ, Han YF, Li SP et al. Evading the strength and ductility trade-off dilemma in titanium matrix composites through designing bimodal grains and micro-nano reinforcements. *Scr Mater* **235**, 115625 (2023).
29. Bai XR, Xie HN, Zhang X et al. Heat-resistant super-dispersed oxide strengthened aluminium alloys. *Nat Mater* **23**, 747–754 (2024).
30. Liu XJ, Duan YP, Guo Y et al. Microstructure design of high-entropy alloys through a multistage mechanical alloying strategy for temperature-stable megahertz electromagnetic absorption. *Nanomicro Lett* **14**, 142 (2022).
31. Wang JM, Jeong SG, Kim ES et al. Material-agnostic machine learning approach enables high relative density in powder bed fusion products. *Nat Commun* **14**, 6557 (2023).
32. Issariyapat A, Visuttipitukul P, Umeda J et al. Refined grain formation behavior and strengthening mechanism of *α*-titanium with nitrogen fabricated by selective laser melting. *Addit Manuf* **36**, 101537 (2020).
33. Dercz G, Matuła I, Zubko M et al. Synthesis of porous Ti-50Ta alloy by powder metallurgy. *Mater Charact* **142**, 124–136 (2018).
34. Tian YY, Zhang LG, Wu D et al. Achieving stable ultra-low elastic modulus in near-β titanium alloys through cold rolling and pre-strain. *Acta Mater* **286**, 120726 (2025).
35. Tao QY, Wang ZW, Chen G et al. Selective laser melting of CP-Ti to overcome the low cost and high performance trade-off. *Addit Manuf* **34**, 101198 (2020).
36. Sharma B, Denand B, Harcuba P et al. Effect of mechanical milling on the harmonic structure development during spark plasma sintering of Ti-5Al-2Sn-4Zr-4Mo-2Cr-1Fe *β*-metastable titanium alloy (*β*-Cez alloy). *J Alloy Compd* **860**, 158483 (2021).
37. Li GD, Liu MW, Lyu SY et al. Simultaneously enhanced strength and strain hardening capacity in FeMnCoCr high-entropy alloy via harmonic structure design. *Scr Mater* **191**, 196–201 (2021).
38. Gao CD, Hu JW, Yao X et al. Competitive microstructural evolution on the soft magnetic and mechanical properties of FeSiB amorphous/nanocrystalline alloys fabricated by laser-beam powder bed fusion. *J Mater Sci Technol* **246**, 28–43 (2026).
39. Zhao W, Xiang HL, Yu RX et al. Effects of laser scanning speed on the microstructure and mechanical properties of 2205 duplex stainless steel fabricated by selective laser melting. *J Manuf Processes* **94**, 1–9 (2023).
40. Riener K, Albrecht N, Ziegelmeier S et al. Influence of particle size distribution and morphology on the properties of the powder feedstock as well as of AlSi10Mg parts produced by laser powder bed fusion (LPBF). *Addit Manuf* **34**, 101286 (2020).
41. Lu SY, Lu SL, Chen B et al. Phase transformation induced twinning in commercially pure titanium: an *in-situ* study. *Scr Mater* **229**, 115350 (2023).
42. Yao ZF, He ML, Yi J et al. High-strength titanium alloy with hierarchical-microstructure design via in-situ refinement-splitting strategy in additive manufacturing. *Addit Manuf* **80**, 103969 (2024).
43. Abbasi M, Kim DI, Guim HU et al. Application of transmitted kikuchi diffraction in studying nano-oxide and ultrafine metallic grains. *ACS Nano* **9**, 10991–11002 (2015).
44. Leung CLA, Marussi S, Atwood RC et al. In situ X-ray imaging of defect and molten pool dynamics in laser additive manufacturing. *Nat Commun* **9**, 1355 (2018).
45. Zhao C, Parab ND, Li XX et al. Critical instability at moving keyhole tip generates porosity in laser melting. *Science* **370**, 1080–1086 (2020).
46. Jeong SG, Karthik GM, Kim ES et al. Architectured heterogeneous alloys with selective laser melting. *Scr Mater* **208**, 114332 (2022).
47. Mandal S, Kumar M, Sengupta P et al. Laser melting of mechanically alloyed FeNi: a study of the correlation between microstructure and texture with magnetic and physical properties. *ACS Omega* **9**, 15650–15662 (2024).
48. Zheng YZ, Huang CC, Li YG et al. Mimicking the mechanical properties of cortical bone with an additively manufactured biodegradable Zn-3Mg alloy. *Acta Biomater* **182**, 139–155 (2024).
49. Huang CC, Wang YZ, Yang F et al. Additively manufactured biodegradable Zn-Mn-based implants with an unprecedented balance of strength and ductility. *Acta Biomater* **196**, 506–522 (2025).
50. Hou YH, Liu B, Liu Y et al. Ultra-low cost Ti powder for selective laser melting additive manufacturing and superior mechanical properties associated. *Opto-Electron Adv* **2**, 180028 (2019). http://doi.org/10.29026/oea.2019.180028.
51. Gu DD, Xia MJ, Dai DH. On the role of powder flow behavior in fluid thermodynamics and laser processability of Ni-based composites by selective laser melting. *Int J Mach Tools Manuf* **137**, 67–78 (2019).
52. Cui DC, Guo BJ, Yang ZS et al. Unraveling microstructure and mechanical response of an additively manufactured refractory TiVHfNbMo high-entropy alloy. *Addit Manuf* **84**, 104126 (2024).
53. Qian BN, Li XQ, Wang Y et al. An ultra-low modulus of ductile TiZrHfTa biomedical high-entropy alloys through deformation induced martensitic transformation/twinning/amorphization. *Adv Mater* **36**, 2310926 (2024).
54. Wu SY, Xu JM, Zou LY et al. Long-lasting renewable antibacterial porous polymeric coatings enable titanium biomaterials to prevent and treat peri-implant infection. *Nat Commun* **12**, 3303 (2021).
55. Wang XQ, Zhang YS, Han WZ. Design of high strength and wear-resistance *β*-Ti alloy via oxygen-charging. *Acta Mater* **227**, 117686 (2022).
56. Seo DI, Lee JB. Localized corrosion and repassivation behaviors of additively manufactured titanium alloys in simulated biomedical solutions. *Npj Mater Degrad* **7**, 44 (2023).
57. Hu N, Xie LX, Liao Q et al. A more defective substrate leads to a less defective passive layer: enhancing the mechanical

strength, corrosion resistance and anti-inflammatory response of the low-modulus Ti-45Nb alloy by grain refinement. *Acta Biomater* **126**, 524–536 (2021).

58. Wang RH, Li J, Bi QJ et al. Crystallographic plane-induced selective mineralization of nanohydroxyapatite on fibrous-grained titanium promotes osteointegration and biocorrosion resistance. *Biomaterials* **313**, 122800 (2025).
59. Qin Y, Jing ZH, Zou D et al. A metamaterial scaffold beyond modulus limits: enhanced osteogenesis and angiogenesis of critical bone defects. *Nat Commun* **16**, 2180 (2025).
60. Herrera P, Hernandez-Nava E, Thornton R et al. Abrasive wear resistance of Ti-6Al-4V obtained by the conventional manufacturing process and by electron beam melting (EBM). *Wear* **524–525**, 204879 (2023). http://doi.org/10.1016/j.wear.2023.204879.
61. Ashkani O, Moazami-Goudarzi M, Abbasi A. Enhanced mechanical properties and wear resistance of titanium by Mn addition. *Mater Today Commun* **44**, 112168 (2025).
62. Ren YJ, Li ZC, Wang QG et al. Effect of Nb content on microstructural evolution, mechanical and tribological properties of in situ alloyed copper-modified titanium produced using laser powder bed fusion. *J Mater Sci Technol* **219**, 257–270 (2025).
63. Ren YJ, Wu H, Agbedor SO et al. Microstructure, mechanical and tribological properties of a Ti-5Cu alloy and a B_4C/Ti-5Cu in situ composite fabricated by laser powder bed fusion. *Mater Charact* **192**, 112217 (2022).
64. Wang QG, Zhao ZY, Liang LX et al. Microstructure and mechanical properties of SiC whiskers modified Ti-39Nb alloy fabricated by laser powder bed fusion. *Mater Sci Eng A* **922**, 147608 (2025).
65. Ayodele OO, Babalola BJ, Olubambi PA. Evaluation of the wear and mechanical properties of titanium diboride-reinforced titanium matrix composites prepared by spark plasma sintering. *Materials* **16**, 2078 (2023).
66. Cao XJ, Liu X, Zhou HB et al. Enhanced properties of titanium matrix composites via in-situ synthesized TiCx and Ti_5Si_3 with network structure. *Mater Chem Phys* **314**, 128849 (2024).
67. Wang WJ, Yang KH, Wang QT et al. Novel Ti-Zr-Hf-Nb-Fe refractory high-entropy alloys for potential biomedical applications. *J Alloy Compd* **906**, 164383 (2022).
68. Liu L, Li SF, Pan D et al. Loss-free tensile ductility of dual-structure Titanium composites via an interdiffusion and self-organization strategy. *Proc Natl Acad Sci USA* **120**, e2302234120 (2023).
69. Mu YK, He LH, Deng SH et al. A high-entropy alloy with dislocation-precipitate skeleton for ultrastrength and ductility. *Acta Mater* **232**, 117975 (2022).
70. Pan QS, Zhang LX, Feng R et al. Gradient cell-structured high-entropy alloy with exceptional strength and ductility. *Science* **374**, 984–989 (2021).
71. Wu D, Hao MY, Zhang TL et al. Heterostructures enhance simultaneously strength and ductility of a commercial titanium alloy. *Acta Mater* **257**, 119182 (2023).
72. Dong Z, Han CJ, Zhao YZ et al. Role of heterogenous microcrostructure and deformation behavior in achieving superior strength-ductility synergy in zinc fabricated via laser powder bed fusion. *Int J Extreme Manuf* **6**, 045003 (2024).
73. Zhai WZ, Bai LC, Zhou RH et al. Recent progress on wear-resistant materials: designs, properties, and applications. *Adv Sci* **8**, 2003739 (2021).

Acknowledgements

This study was supported by the following funds: (1) National Key Research and Development Program of China (2023YFB4605800); (2) Hunan Provincial Natural Science Foundation of China (2025JJ30015); (3) The Natural Science Foundation of China (U24A20120, 52475362, 52275395); (4) The Science and Technology Innovation Program of Hunan Province (2023RC3046); (5) Young Elite Scientists Sponsorship Program by CAST (2020QNRC002); (6) Central South University Innovation-Driven Research Programme (2023CXQD023); (7) JiangXi Provincial Natural Science Foundation of China (20224ACB204013); (8) The Project of State Key Laboratory of Precision Manufacturing for Extreme Service Performance, Central South University; (9) The Fundamental Research Funds for the Central Universities of Central South University (CX20240012).

Competing interests

The authors declare no competing financial interests.

Supplementary information

Supplementary information for this paper is available at
https://doi.org/10.29026/oea.2026.250043